



## Intense deformation and fragmentation of two droplet collision at high Weber numbers

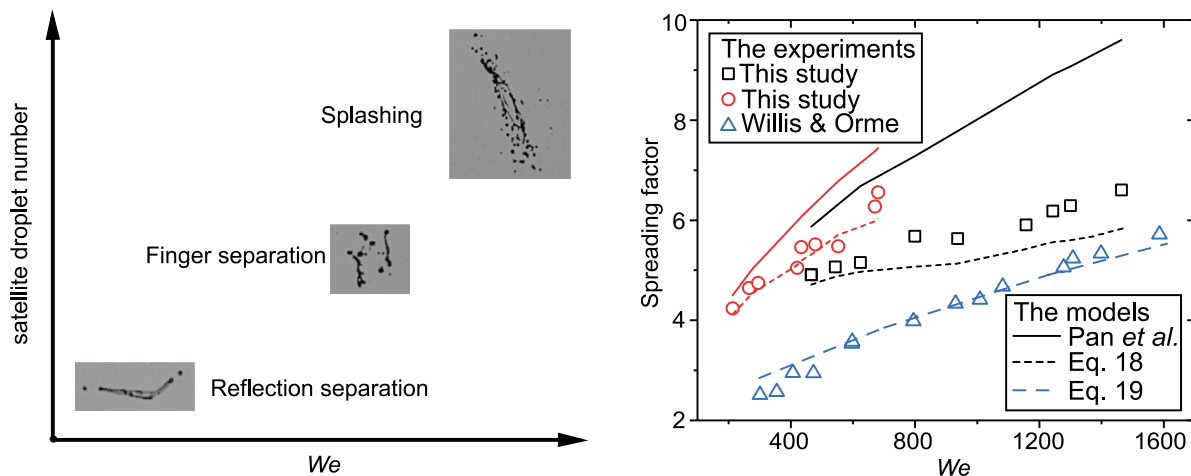
Dongdong Zhou, Xiufang Liu, Song Yang, Yu Hou, Xin Zhong \*

*State Key Laboratory of Multiphase Flow in Power Engineering, Xi'an Jiaotong University, Shaanxi 710049, China*

*Division of Refrigeration and Cryogenic Engineering, School of Energy and Power Engineering, Xi'an Jiaotong University, Shaanxi 710049, China*



### GRAPHICAL ABSTRACT



### ARTICLE INFO

**Keywords:**  
Droplet collision  
High Weber number  
Maximum deformation  
Fragmentation

### ABSTRACT

Droplet collision is common in nature and industrial processes, while understanding of the phenomena at high Weber numbers is not as comprehensive as the one at low Weber numbers. We experimentally investigate the collision dynamics of two droplets at high  $We$  ranging from 200 to 2000 by adopting pure water and pure ethanol droplets. Four distinct droplet collision regimes in the order of increasing deformation and fragmentation are reflection separation, finger separation, stretching separation and splashing. Due to the larger inertia force and lower viscous force, water droplet collision is easier to form finger separation and splashing regimes than ethanol droplets under the same  $We$ . The reinforcement of viscous force and surface tension weakens droplet deformation and fragmentation, and further changes droplet collision regime. Due to the viscous dissipation ratio of droplet at the maximum spread moment as a function of Ohnesorge number ( $Oh$ ), the model of the maximum spread factor of coalesced droplet is different under various  $Oh$ . For a low  $Oh$ , a new formula of the maximum spread factor is proposed by optimizing the maximum spread time in the viscous dissipation model based on energy conservation, which agrees well with the experiment. For a high  $Oh$ , the formula of the maximum spread factor is developed by using the viscous dissipation ratio, and it is consistent with the experiment as the viscous dissipation ratio is 0.8.

\* Corresponding author.

E-mail address: [zhongxin0521@xjtu.edu.cn](mailto:zhongxin0521@xjtu.edu.cn) (X. Zhong).

## 1. Introduction

Droplet collision at high Weber number  $We$  ( $> 200$ ) produces intense separation and fragmentation [1–3], in contrast to the lower breaking extent at low  $We$  which has been extensively studied [4–9]. Fragmentation of droplet changes the spatial distribution, size and number of satellite droplets, affecting the efficiency of droplet-based industrial fields, such as combustion [10], spraying [11], and oil–water treatment [12]. Therefore, understanding the dynamics of droplet collision at high  $We$  is crucial for the safety operation as well as improving the efficiency of droplet-based equipment.

Fragmentation of droplet is affected by many factors [13–18], among which the effects of inertia [19], surface tension [20] and viscous forces [21] are significant.  $We$  and Reynolds number  $Re$  express the relative importance of inertia to surface tension forces, and inertia to viscous forces respectively. The normally adopted method of increasing the inertia force in plenty of experimental studies is to increase droplet velocity [22–24]. In the region  $We < 30$ , droplet collision exhibits coalescence and bouncing [22,25]. Huang and Pan [26] found that the transition from coalescence to bouncing was controlled by the gas draining dynamics in the inter-droplet film, which is influenced by the two-phase Ohnesorge number, the Ohnesorge number of liquid and the Hamaker constant. They developed a thickness-based model to predict the transition of coalescence and bouncing, and found that the transitional  $We$  is universally 4. In addition, Chen and Yang [27] reproduced numerically the gas film between two droplets by a thickness-based refinement technique, and simulated the phenomena of coalescence and bouncing. When  $30 < We < 140$ , droplet collision exhibited successively reflection separation, coalescence, stretching separation and bouncing as increasing the impact parameter  $B$ . Moqaddam et al. [28] simulated the separation of droplet by entropic lattice Boltzmann. They found that the droplet separation for a low  $B$  is dominated by the mechanism of end-pinch [29], while it is governed by the one of capillary-wave in the high  $B$  region [30]. Planchette et al. [31] found that the fragmentation criterion can be reduced to the well-known Rayleigh criterion for capillary instability under head-on collision. Due to the reduced normal component of the impact inertia, the component of the internal liquid motion responsible for separation was correspondingly reduced [29]. Therefore, droplet collision exhibited coalescence for a medium  $B$ . Based on the analogy of droplets and liquid springs, and the use of Rayleigh criterion, Planchette et al. [32] developed a general model for predicting the threshold velocity of reflection separation for head-on collision. The predicted results of three types of droplet collisions with different liquids and sizes agreed well with the experimental ones. Baumgartner et al. [33] investigated the off-center collision and found a universal model for predicting the onset of stretching separation. The model is valid for a wide range of liquid properties without any parameter correction. When  $We$  was increased to the medium region ( $140 < We < 200$ ), droplet collision exhibited reflection separation at a low  $B$ , and bouncing at a high  $B$ , while stretching separation at a medium  $B$ . Further increasing  $We$  enabled droplet collision to show intensified fragmentation [34]. Pan et al. [1] studied head-on collision of two equal-sized water droplets when  $We$  was up to 5100. At a high  $We$ , fingering lamella caused by Rayleigh–Taylor instability and subsequent splashing due to fragmentation occurred on the collision plane. However, with a further increase of  $We$ , droplet splashed immediately before spreading out. Willis and Orme [2,3] experimentally studied the droplet collision at  $We$  up to 4661. The study showed that time period of oblate oscillation was relatively constant with  $We$  and viscosity, while the time period of prolate oscillation increased exponentially with the square of  $Re$ . In addition, they also found that the dimensionless area of the coalesced droplet varies with viscosity and  $We$  at the moment of maximum deformation, indicating that the viscous dissipation energy increased with increasing viscosity.

Droplet properties which affect inertia force, viscous force, and surface tension, are decisive factors to the collision outcomes. For instance, hydrocarbon droplet collision exhibited the bouncing regime, which, however, did not occur in water droplet collision [35]. Brenn et al. [36] conducted a comparative study on the collision of isopropanol and acetone droplets, and they found that a lower viscosity is easier to enable separation and generation of more satellite droplets. Gotaas et al. [37] proposed a theoretical model for predicting the reflection separation and stretching separation of high viscosity fluids. The results showed that the increase of droplet viscosity led to a transition from coalescence to separation toward a higher  $We$  resulting from the higher viscous dissipation. The experimental study of Al-Dirawi et al. [38] showed that the coalescence/stretching separation transition was inertial for an order-of-magnitude-wide range of Ohnesorge numbers, that is, independent of viscosity. They found that stretching separation only occurred when the stretched droplet exceeded a critical dimensionless length, and based on this criterion, they developed a simple but robust model to capture the coalescence/stretching separation transition. The proposed model without arbitrarily chosen free parameters was consistent with their experiments as well as the ones of reported literatures. In respect to surface tension, Sedano et al. [39] numerically investigated collision of droplets with various surface tensions. A lower surface tension is conducive for the emergence of reflection separation and stretching separation and hence a larger number of satellite droplets. Similar findings were reported by Shlegel et al. [40] that the critical  $We$  for the onset of droplet separation regime decreased by 67% with a twofold decrease of surface tension. It was also found that a decrease in surface tension reduced the impact velocity required for secondary atomization of droplets and the size of satellite droplets, thus enhanced the formation of fine droplets.

Hitherto, most studies of droplet collision mainly focused on droplet coalescence, bouncing and separation which emerging at low  $We$  [4–9], and the studies on droplet deformation and fragmentation normally occurring at high  $We$  [1–3] are less. Surface tension and viscosity are closely related to droplet deformation and fragmentation which enlarge liquid–gas interface of droplets and are thus vital for heat transfer in spray and combustion fields. Based on careful experimental configuration, we investigate the collision dynamics of ethanol droplets and water droplets in a relatively high  $We$  region ( $200 \leq We < 2000$ ). It is found that droplet collision exhibits distinct dynamic regimes as  $We$  is higher than 700. The extent of droplet deformation and fragmentation of each collision regime, and the effects of impact parameters as well as liquid properties are revealed. In addition, we improve the model of the maximum deformation of both water and ethanol droplets through optimizing the formula of the maximum spread time. This study reveals the collision dynamics of droplets at high  $We$ , which could enrich the knowledge of droplet collision dynamics and provide theoretical basis for optimization of droplet-based applications.

## 2. Experimental methods

### 2.1. Experimental setup

The schematic diagram of the experimental setup of droplet collision is shown in Fig. 1. The solutions of droplet were pure water and ethanol. The physical properties of the two solutions are listed in Table 1. The solution stored in the surge tank is driven by high-pressure nitrogen into two droplet generators, and then is ejected to form regular and consecutive droplets, namely a droplet train, under the action of periodic vibration of piezoelectric ceramic piece controlled by a function waveform generator. The two droplet generators are installed on the adjustable brackets which can be rotated to regulate the collision angle of droplet trains. The velocity of the droplet train can be controlled within 8 to 24 m/s by controlling the pressure of high-pressure nitrogen. The diameter of the droplet ranges from 0.14 to 0.32 mm. The collision process is recorded by the high-speed camera (FASTCAM Mini

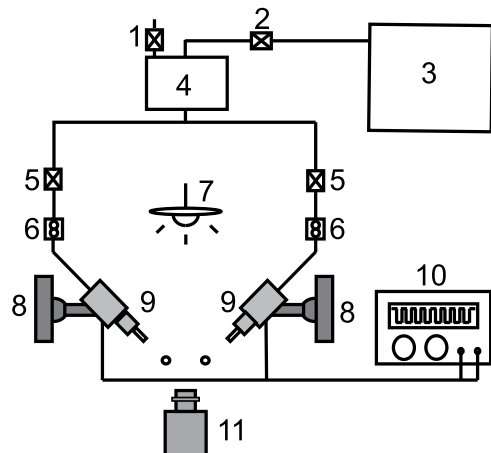


**Fig. 1.** Schematic diagram of the experimental setup of droplet collision. 1 - relief valve, 2 - pressure stabilizing valve, 3 - pressurized gas, 4 - surge tank, 5 - regulating valves, 6 - pressure gages, 7 - light source, 8 - adjustable brackets, 9 - droplet generators, 10 - function waveform generator, 11 - high-speed camera.

**Table 1**

Density  $\rho_l$ , dynamic viscosity  $\mu_l$  and surface tension  $\sigma$  of pure water and pure ethanol liquid under room temperature.

Liquid	$\rho_l$ kg/m <sup>3</sup>	$\mu_l$ Pa · s	$\sigma$ N/m
Water	998.2	$1.0 \times 10^{-3}$	$7.27 \times 10^{-2}$
Ethanol	789.75	$1.19 \times 10^{-3}$	$2.23 \times 10^{-2}$

AX100) with a 60 mm f/2.8D Nikon lens with resolution and frame rate  $f$  set at  $384 \times 384$  and 20,000 fps, respectively. The software of Photron FASTCAM Viewer 4 was used for post-processing of the collision snapshots.  $t = 0$  ms was defined as the previous moment of the first contact of two droplets.

## 2.2. Description of droplet collision

The schematic diagram of droplet collision is shown in Fig. 2. Two equal-sized droplets collide with the collision angle  $\theta_1$  and  $\theta_2$ , and the initial velocities  $u_{01}$  and  $u_{02}$  respectively, where  $\theta_1$  and  $\theta_2$ , the angle between the gravity force and impact direction, range from  $0^\circ$  to  $90^\circ$ . The Weber number  $We$ , Reynolds number  $Re$ , Capillary number  $Ca$ , Ohnesorge number  $Oh$  and impact parameter  $B$  are used to describe the initial collision conditions, and the formulas are respectively

$$We = \frac{\rho_l u_r^2 D_0}{\sigma} \quad (1)$$

$$Re = \frac{\rho_l u_r D_0}{\mu_l} \quad (2)$$

$$Ca = \frac{We}{Re} = \frac{\mu_l}{\sigma} u_r \quad (3)$$

$$Oh = \frac{\sqrt{We}}{Re} = \frac{\mu_l}{\sqrt{\rho_l \sigma D_0}} \quad (4)$$

and

$$B = \frac{b}{D_0} \quad (5)$$

where  $u_r$  and  $D_0$  are the relative velocity and initial diameter of droplets respectively, and  $b$  is the distance between the two droplet centers on a plane perpendicular to the relative velocity vector.  $Ca$  and  $Oh$  represent the relative importance of viscous force to surface tension force.  $B$  represents the relative positions of colliding droplets, and  $0 \leq B < 1$ .  $0 < B < 1$  indicates off-center collision, and  $B = 0$  indicates head-on collision.

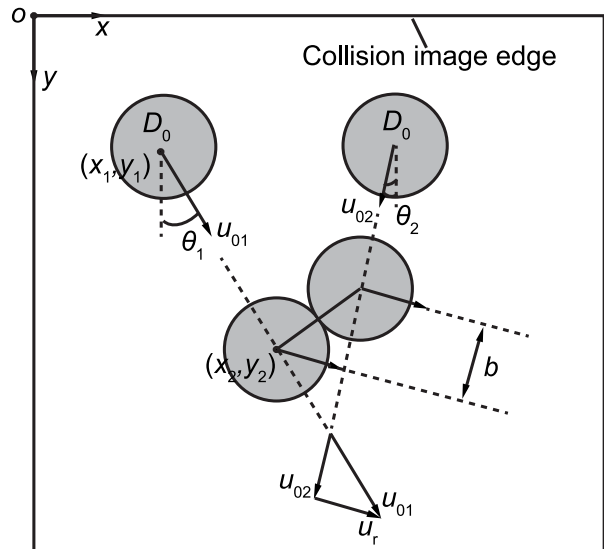


**Fig. 2.** Schematic diagram of collision of two equal-sized droplets with different initial magnitudes of velocity and collision angles.

The velocity  $u$  of the droplet train is

$$u = f \sqrt{(x_1 - x_2)^2 + (y_1 - y_2)^2} \quad (6)$$

where  $(x_1, y_1)$  and  $(x_2, y_2)$  are the two coordinates of a single droplet at random two adjacent moments prior to droplet collision respectively (see Fig. 2). The upper left vertex of collision image is the origin  $o$  of cartesian coordinate system. The collision angle  $\theta$  of droplet train is

$$\theta = \arctan \left( \frac{y_1 - y_2}{x_1 - x_2} \right) \quad (7)$$

Once  $u$  and  $\theta$  are determined,  $u_r$  of the two droplets can be obtained by the geometric calculation of the velocity triangle shown in Fig. 2.

## 2.3. Experimental data

The droplet spread factor  $\alpha = L_d/D_0$  is used to describe the deformation during collision.  $L_d$  is the instantaneously length of colliding droplets, which is measured under two conditions. It indicates the instantaneously length  $L_{cd}$  of a coalesced droplet (see Fig. 3(a)).  $\alpha_{max} = L_{cd\_max}/D_0$  is the maximum spread factor for the coalesced droplet, where  $L_{cd\_max}$  is the maximum length. In addition,  $L_d$  also denotes the instantaneously length  $L_{bd}$  of the droplet after it breaks (see Fig. 3(b)).

The droplet diameter ratio  $\beta = D_v/D_0$  is used to describe the size of the satellite droplet, where  $D_v$  is the equivalent spherical volume diameter. The satellite droplet shape captured by the camera on the collision plane is two-dimensional (2D), and we obtained its volume by recovering it to a three-dimensional (3D) profile. The droplets are found to be either near-spherical-shaped or disk-shaped, which can be distinguished by the snapshots captured by the camera. We employed the aspect ratio  $\gamma = b/a$  to present the irregularity of a 2D droplet shape deviating from a circle, where  $b$  and  $a$  are the diameter along the major and minor axes of the droplet, respectively. The 2D shape represents a circle at  $\gamma = 1$ , and represents an ellipse at  $\gamma > 1$ . For a near-spherical morphology, we assume that the cross-sectional area of the droplet perpendicular to the collision plane is circularly-shaped and its diameter is  $a$ . When the 3D droplet recovered from the 2D profile on the collision plane is a sphere or an ellipsoid, its volume  $V = \pi a^3 \gamma / 6$ . When it is a round disk or an oval disk,  $V = \pi a^2 \gamma \delta / 4$ , where  $\delta$  is the thickness of the disk. As a result,  $D_v = \sqrt[3]{(3V)/(4\pi)}$ , which represents the diameter of a sphere with its volume equivalent to that of the droplet.

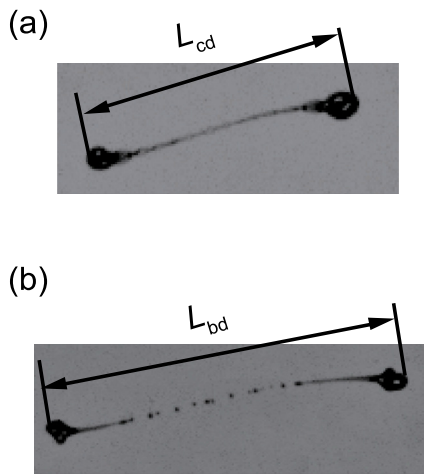


**Fig. 3.** Measurement of droplet spreading length  $L_d$ , including (a)  $L_{cd}$  for the coalesced droplet and (b)  $L_{bd}$  after it breaks.

### 3. Results and discussion

#### 3.1. Droplet collision regimes

Both water droplet collision and ethanol droplet collision exhibit four regimes under various  $We$  and  $B$ , which are reflection separation (RS), stretching separation (SS), finger separation (FS) and splashing (SP). As shown in Fig. 4(a), at  $We = 520$ ,  $B = 0.04$  and  $D_0 = 0.18$  mm, where the corresponding  $Re$  is 1080, the two droplets approaching to each other begin to contact at  $t = 0.05$  ms. The merged droplet is then extended vertically, forming a disk-shaped liquid film at  $t = 0.15$  ms. The edge of the liquid film has a large curvature, which enables the liquid film to shrink inward due to surface tension. The shrinking liquid continuously converges to the center, and then at  $t = 0.45$  ms, it is squeezed to spread horizontally. From  $t = 0.6$  ms and onwards, the horizontal spreading motion enables a few satellite droplets to be detached from the two ends, and the droplet is split into three main portions. This regime is indicated as reflection separation (RS).

At  $We = 500$ ,  $B = 0.72$  and  $D_0 = 0.20$  mm, where the corresponding  $Re$  is 1061, the two ethanol droplets collide at 0.05 ms, after which the coalesced droplet is extended, forming a dumbbell shape at 0.25 ms due to the original motion of the two droplets. The dumbbell-shaped droplet keeps extending, such that the intermediate ligament becomes increasingly narrow, as shown by the snapshots in Fig. 4(b) at 0.35 and 0.45 ms. At 0.70 ms, the ligament is torn and numerous satellite droplets are produced. This is indicated as stretching separation regime (SS).

At  $We = 1140$ ,  $B = 0.40$  and  $D_0 = 0.20$  mm, where the corresponding  $Re$  is 1600, as shown in Fig. 4(c), the ethanol droplet colliding at  $t = 0.05$  ms are then deformed to be a liquid film at  $t = 0.30$  ms. Meanwhile, finger-like ridges appear at the rim of the liquid film, which indicates the occurrence of Rayleigh–Taylor instability or rim instability [41–43]. Later at  $t = 0.35$  ms, the liquid film begins to contract due to surface tension, and it splits to plenty of satellite droplets, which is indicated as the regime of finger separation (FS).

At  $We = 1915$ ,  $B = 0.18$  and  $D_0 = 0.26$  mm, where the corresponding  $Re$  is 2392, as shown in Fig. 4(d), the colliding ethanol droplets form a thin liquid film with a greater number of finger-like ridges at its rim at  $t = 0.10$  ms. However, different from the case at  $t = 0.30$  ms in Fig. 4(c), the liquid film at  $t = 0.10$  ms continues to spread out, and later the finger-like ridges begin to split into a large number of small droplets along with the spreading, during which the central liquid remains as a film, as exemplified by the snapshots at 0.35 ms and 0.40 ms. This is denoted as the splashing regime (SP).

**Fig. 5** shows the evolutions of  $\alpha$  with  $t$  under various regimes.  $\alpha$  of both RS and FS increase first and then decrease, and reaches the maximum at  $t = 0.2$  ms. In addition, it can be seen from Fig. 5 that  $\alpha$  at  $t = 0.3$  ms is close to its maximum at  $t = 0.2$  ms for RS and FS regimes. For SP and SS,  $\alpha$  keeps increasing with  $t$ , so it reaches the maximum at  $t = 0.3$  ms. Therefore, to exhibit the deformation and fragmentation extent of the various collision regimes, we plot  $\alpha$  and the number  $N$  of satellite droplets for the RS, FS, SP and SS regimes under various  $We$  and  $B$  at  $t = 0.30$  ms in Fig. 6(a) to (d). Fig. 6(a) and (b) show that as  $We$  increases, droplet collision exhibits the regimes of RS, FS and SP under the near head-on collision ( $B = 0.05$ ), and their  $\alpha$  and  $N$  both increase, suggesting that the deformation and fragmentation of the SP regime are the strongest, followed by the FS and RS regimes. Under the off-center collision ( $B = 0.6$ ), with the increase of  $We$ , droplet collision exhibits SS regime first and then SP regime, as shown in Fig. 6(c) and (d), and their  $\alpha$  and  $N$  also increase, suggesting that the deformation and fragmentation of SP regime are stronger than those of SS regime. In addition, Fig. 6(a) and (c) show that  $\alpha$  of the SS regime is larger than that of the RS and FS regimes under the same  $We$  range, indicating that the deformation of the SS regime is more intense. Fig. 6 also shows that  $\alpha$  and  $N$  of the SP regime at  $B = 0.6$  are greater than those at  $B = 0.05$ , indicating that the deformation and fragmentation under the off-center collision are stronger than those under the near head-on collision. It can be concluded that the extent of droplet deformation and fragmentation increases with  $We$ , and the SP regime features the strongest deformation and fragmentation.

#### 3.2. Phase diagrams of collision regimes

We plot the phase diagrams of collision regimes depicted by  $B$  and  $We$ , and by  $B$  and  $Re$  respectively for pure water and ethanol droplets in Fig. 7. As shown in Fig. 7(a) and (b), for the water droplets, at a relatively small  $B$ , increasing  $We$  and the corresponding  $Re$  lead to the regime transition from RS to FS and to SP. At a higher  $B$ , droplet separation after collision occurs for all the  $We$  and  $Re$  in this study. The critical  $B$  for the emergence of SS regime first decreases and then increases with  $We$  and  $Re$ .

The phase diagrams for the ethanol droplets are similar to those of the water droplets, as shown in Fig. 7(c) and (d). The difference is that for ethanol droplet collision, the critical  $We$  is increased, while the corresponding  $Re$  is decreased for the commencement of FS and SP regime. Moreover, the range of  $We$  is expanded, but the one of the corresponding  $Re$  is narrowed for the formation of the FS regime. The different droplet properties determine the different combined effects of inertia force, surface tension and viscous force which further affect the collision result. As listed in Table 1,  $\rho_l$  and  $\sigma$  are higher, while  $\mu_l$  is lower for water than those of ethanol. For the same  $We$ ,  $Re$  of the water droplet is much larger than that of the ethanol droplet, suggesting that the water droplet possesses a relatively higher inertia force and lower viscous force. Therefore, water droplet collision is easier to form FS and SP, which exhibit stronger deformation and separation, under the same  $We$  range. In addition, in the medium and higher region of  $We$  and  $Re$ , Fig. 7 shows that the critical  $B$  for the SS regime of the water droplet is lower than that of the ethanol droplet. The occurrence of SS regime depends on the competition between the surface energy of the interaction region and the portion of initial kinetic energy responsible for the stretching and separation of the coalesced droplet [30]. Under the same  $We$  indicating that the water and ethanol droplets have the same ratio of initial kinetic energy to surface energy,  $Re$  of the ethanol droplet is smaller, suggesting that the consumption of initial kinetic energy by viscous dissipation for the ethanol droplet is greater. Therefore, water droplet collision maintains a higher kinetic energy for stretching, and hence is more likely to form SS regime than ethanol droplet collision at a relatively high  $We$ .

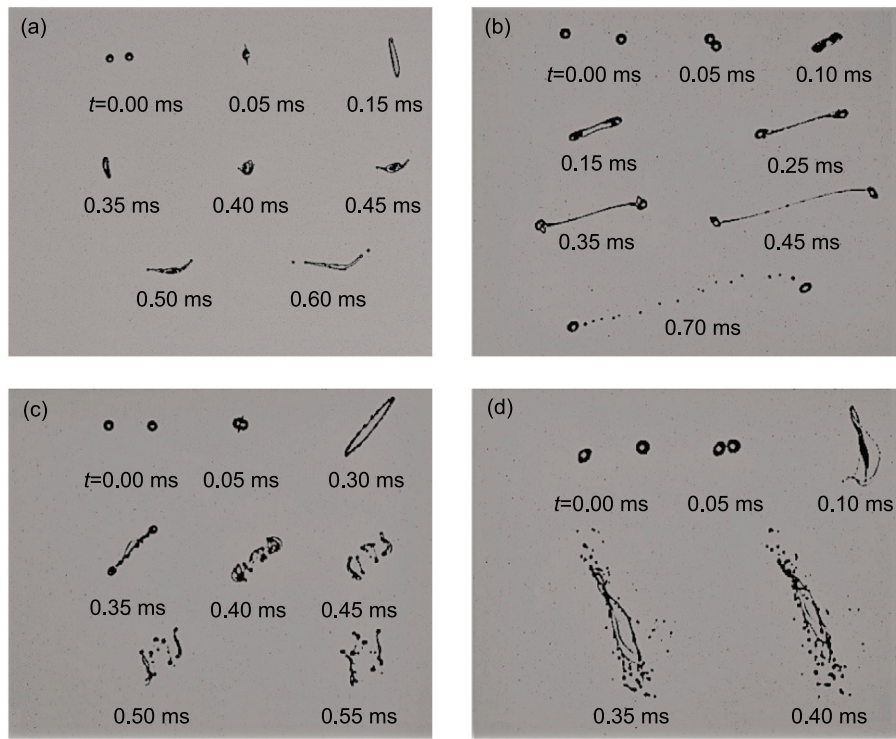


**Fig. 4.** (a) At  $We = 520$ , impact parameter  $B = 0.04$  and droplet initial diameter  $D_0 = 0.18$  mm, where the corresponding  $Re$  is 1080, the reflection separation regime (RS) of two colliding ethanol droplets. (b) At  $We = 500$ ,  $B = 0.72$ ,  $D_0 = 0.20$  mm, and the corresponding  $Re = 1061$ , the stretching separation regime (SS) of two colliding ethanol droplets. (c) At  $We = 1140$ ,  $B = 0.40$ ,  $D_0 = 0.20$  mm, and the corresponding  $Re = 1600$ , the finger separation regime (FS) of two colliding ethanol droplets. (d) At  $We = 1915$ ,  $B = 0.18$ ,  $D_0 = 0.26$  mm, and the corresponding  $Re = 2392$ , the splashing regime (SP) of two colliding ethanol droplets. Also see Video S1 of Supporting information for the RS, FS, SS and SP collision regimes of pure ethanol droplets.

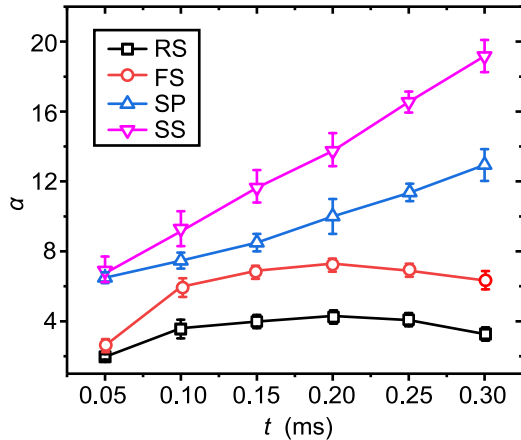


**Fig. 5.** The spread factor  $\alpha$  of the colliding droplets versus time  $t$  under various regimes. RS, FS, SP, SS are the abbreviations of the regimes of reflection separation, finger separation, splashing and stretching separation, respectively.

### 3.3. Collision dynamics under the same $We$ and $Re$

Effects of liquid properties on droplet collision can be reflected by the deformation and fragmentation of two colliding droplets. Fig. 8 (a1) to (a4) show the spread factor  $\alpha$  versus time  $t$ . Fig. 8 (b1) to (b4) show the size distribution of droplets after collision under various  $We$ ,  $Re$  and  $B$ . It shows the relationship between  $\beta$  of satellite droplets and its number  $N$ . The range of  $\beta$  is divided into four levels of  $0 \sim 0.2$ ,  $0.2 \sim 0.5$ ,  $0.5 \sim 1.0$  and  $1.0 \sim 1.26$ .

At  $We = 1000$ ,  $B = 0.05$  and  $D_0 = 0.18$  mm for ethanol droplets and  $D_0 = 0.28$  mm for water droplets, as shown in Fig. 8 (a1),  $\alpha$  of the water droplet increases with  $t$ , while for the ethanol droplet it increases first

and then decreases, in accordance with the droplet contraction occurring at a latter moment of the FS regime (see Fig. 4(c)).  $\alpha$  of the water droplet is larger than that of the ethanol droplet, suggesting greater deformation. Fig. 8 (b1) shows that the total  $N$  of the water droplet is greater than that of the ethanol droplet. Water droplet collision results in large  $N$  in the range of  $\beta < 1.0$ , suggesting production of plenty of small satellite droplets. For the ethanol droplet which does not break at 0.3 ms, its  $1.0 < \beta < 1.26$  denotes the size of the coalesced droplet.

The droplet collision under off-center condition with  $B = 0.6$  is generally similar to that under the near head-on condition of  $B = 0.05$ . Fig. 8 (a2) shows that for  $B = 0.6$ ,  $We = 1000$  and  $D_0 = 0.18$  mm for ethanol droplets and  $D_0 = 0.28$  mm for water droplets,  $\alpha$  increases with  $t$ , and it is larger for the water droplet and smaller for the ethanol droplet. Resembling to the case shown in Fig. 8 (b1), Fig. 8 (b2) shows that  $N$  of the water droplet is much larger than that of the ethanol droplet at  $t = 0.40$  ms. At the same  $We$  of 1000, the corresponding  $Re$  is 4184 and 1400 for the water and ethanol droplets, indicating that the relative role of viscous dissipation which consumes initial kinetic energy is enhanced for the ethanol droplet. Therefore, the water droplet collision exhibited the greater extent of deformation and fragmentation.

Fig. 8 (a3) shows that  $\alpha$  of the ethanol droplet is larger than that of the water droplet for  $Re = 2200$ ,  $B = 0.05$  and  $D_0 = 0.16$  mm for ethanol droplets and  $D_0 = 0.25$  mm for water droplets, suggesting that its deformation is more intense. Fig. 8 (b3) shows that at  $t = 0.40$  ms,  $N$  of the ethanol droplet is much larger than that of the water droplet which fails to break at this moment, indicating that fragmentation of the ethanol droplet is more intense. Fig. 8 (a4) and (b4) show respectively that the evolution of  $\alpha$  and the distribution of  $N$  at  $t = 0.40$  ms for  $Re = 2200$ ,  $B = 0.6$  and  $D_0 = 0.16$  mm for ethanol droplets and  $D_0 = 0.25$  mm for water droplets.  $\alpha$  increases with  $t$ , and it is higher for the ethanol droplet. Fig. 8 (b4) shows that only the ethanol droplet breaks, and its  $\beta$  is located at  $0 \sim 1$ . At  $Re = 2200$ ,  $We$  of the water and ethanol droplets is 271 and 1717 respectively, suggesting an enhanced

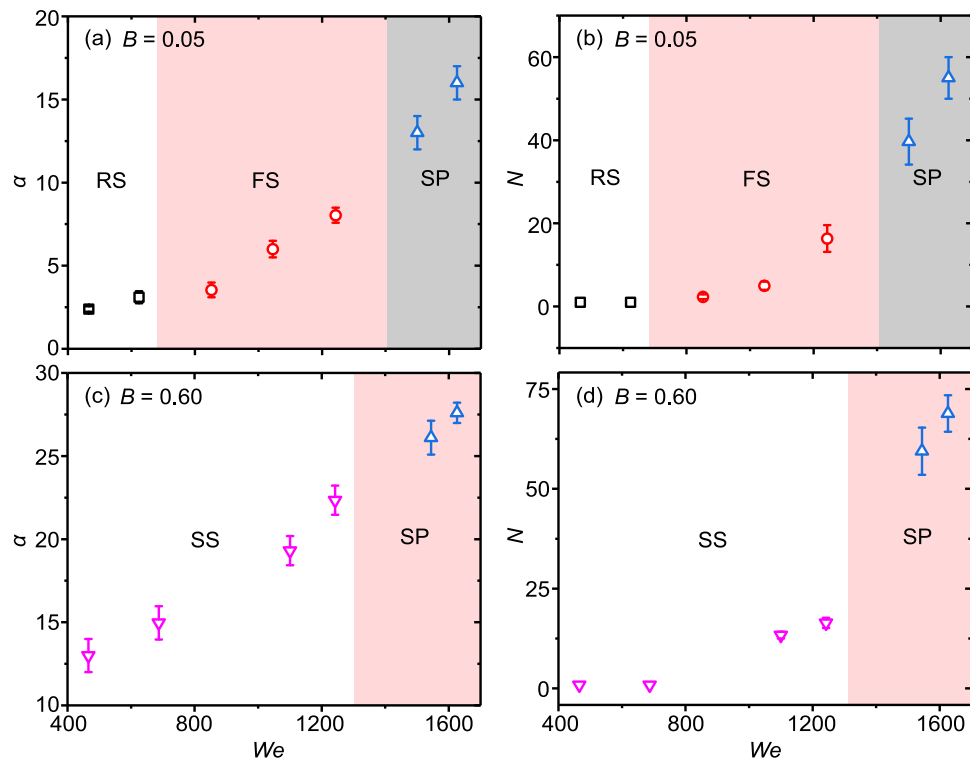


**Fig. 6.** At time  $t = 0.30$  ms and impact parameter  $B = 0.05$ , (a) the spread factor  $\alpha$  of colliding droplets and (b) the number  $N$  of satellite droplets versus  $We$ . At  $t = 0.30$  ms and  $B = 0.6$ , (c)  $\alpha$  and (d)  $N$  versus  $We$ . RS, FS, SS and SP stand for reflection separation, finger separation, stretching separation and splashing respectively.

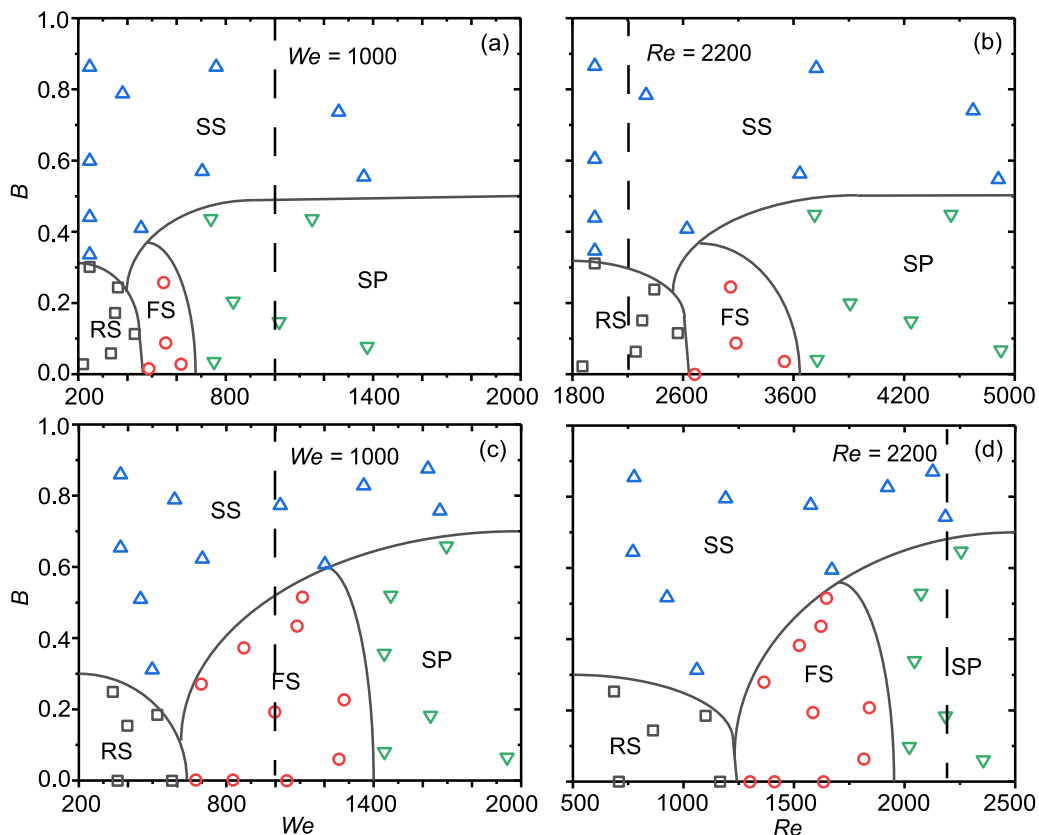


**Fig. 7.** Phase diagram depicted by (a)  $B$  and  $We$  and (b)  $B$  and  $Re$  for water droplet collision. Phase diagram depicted by (c)  $B$  and  $We$  and (d)  $B$  and  $Re$  for ethanol droplet collision. RS, FS, SS and SP stand for reflection separation, finger separation, stretching separation and splashing respectively.

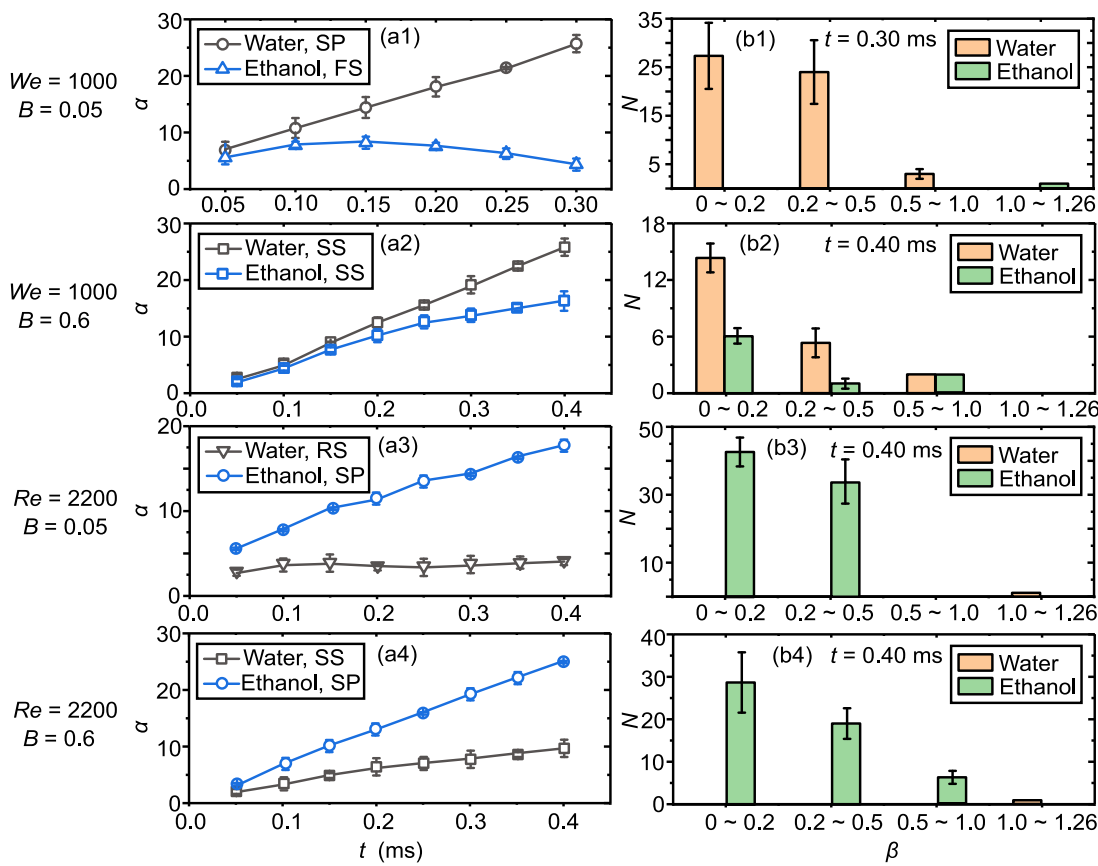


**Fig. 8.** At  $We = 1000$ , impact parameter  $B = 0.05$  and the droplet initial diameter  $D_0 = 0.18$  mm for ethanol droplets and  $D_0 = 0.28$  mm for water droplets, (a1) the spread factor  $\alpha$  of the colliding droplets versus time  $t$  and (b1) the number  $N$  of satellite droplet versus the diameter ratio  $\beta$  at  $t = 0.30$  ms. At  $We = 1000$ ,  $B = 0.6$  and  $D_0 = 0.18$  mm for ethanol droplets and  $D_0 = 0.28$  mm for water droplets, (a2)  $\alpha$  versus  $t$  and (b2)  $N$  versus  $\beta$  at  $t = 0.40$  ms. At  $We = 2200$ ,  $B = 0.05$  and  $D_0 = 0.16$  mm for ethanol droplets and  $D_0 = 0.25$  mm for water droplets, (a3)  $\alpha$  versus  $t$  and (b3)  $N$  versus  $\beta$  at  $t = 0.40$  ms. At  $We = 2200$ ,  $B = 0.6$  and  $D_0 = 0.16$  mm for ethanol droplets and  $D_0 = 0.25$  mm for water droplets, (a4)  $\alpha$  versus  $t$  and (b4)  $N$  versus  $\beta$  at  $t = 0.40$  ms.

relative role of surface tension for the water droplet. Therefore, the ethanol droplet collision exhibits more intense fragmentation due to the lower surface tension restraint.

In Fig. 8,  $We$  and  $Re$  are alternatively set constant to reveal respectively the effect of viscous force and surface tension on droplet deformation and fragmentation. The increase of viscous force and surface tension hinders droplet deformation and fragmentation, and further affects the regime of droplet collision. For example, at  $We = 1000$  and  $B = 0.05$ , the larger viscous force causes ethanol droplet collision to exhibit the FS regime, while water droplet collision exhibits the SP regime which features the most intense deformation and fragmentation among all the regimes. At  $Re = 2200$  and  $B = 0.05$ , the larger surface tension enables water droplet collision to show RS regime, while ethanol droplet collision shows SP regime.

#### 3.4. Optimization of the modeling on droplet maximum deformation

Herein we aim at developing an improved model for the maximum deformation of two droplet collision. Based on energy conservation, Pan et al. [1] modeled the maximum spread factor  $\alpha_{\max}$  of droplet collision for water and water-57% glycerine droplets at  $We > 200$  by

$$\left(\frac{1}{Ca} + \frac{1}{2}\right)\alpha_{\max}^3 - \left(\frac{4}{Ca} + \frac{Re}{12}\right)\alpha_{\max} + \frac{4}{3Ca} = 0 \quad (8)$$

Herein we reevaluate the viscous dissipation during droplet collision to optimize the model of  $\alpha_{\max}$ . Fig. 9 shows the schematic diagram of the collision of two equal-sized droplets with the same initial magnitude of velocity  $|\vec{u}_0|$  at  $B = 0$ .  $\vec{u}_0$  can be decomposed into  $\vec{u}_{x0}$  driving droplet to collide in  $x$ -direction, and  $\vec{u}_{y0}$  enabling the downward motion of the

droplet, respectively. Therefore, the total initial kinetic energy  $E_{k0} = \pi\rho_1 D_0^3 u_0^2/6$  of the droplets can be divided into the initial horizontal kinetic energy  $E_{kx0} = \pi\rho_1 D_0^3 u_{x0}^2/6$  and the initial vertical kinetic energy  $E_{ky0} = \pi\rho_1 D_0^3 u_{y0}^2/6$ , namely  $E_{k0} = E_{kx0} + E_{ky0}$ . At  $t_{\max}$  when the coalesced droplet spreads to  $L_{\max}$ , the coalesced droplet evolves into a disk of thickness  $\delta$  where it stops spreading and its kinetic energy  $E_{kx}$  in  $x$ -axis direction is zero. The work done by gravity on the droplets increases their kinetic energy in  $y$ -direction and has negligible effect on the droplet collision. Therefore, considering energy conservation from the moment right before contact at  $t = 0$  ms to  $t_{\max}$  along  $x$ -direction, we have

$$E_{kx0} + E_{s0} = E_s + E_{dis} \quad (9)$$

where  $E_{s0} = 2\pi D_0^2 \sigma$  is the surface energy of the colliding droplets at  $t = 0$  ms.  $E_s = A\sigma$  is the surface energy of the coalesced droplet at  $t_{\max}$ , where  $A$  is the droplet area.  $E_{dis}$  is the viscous dissipation energy from 0 ms to  $t_{\max}$ . The experimental  $E_{dis}$  can be calculated by

$$E_{dis} = E_{kx0} + E_{s0} - E_s \quad (10)$$

According to conservation of mass,

$$\delta = \frac{4D_0^3}{3L_{\max}^2} \quad (11)$$

Therefore,  $E_s$  is

$$E_s = \left(\frac{4\pi D_0^3}{3L_{\max}} + \frac{\pi L_{\max}^2}{2}\right)\sigma \quad (12)$$

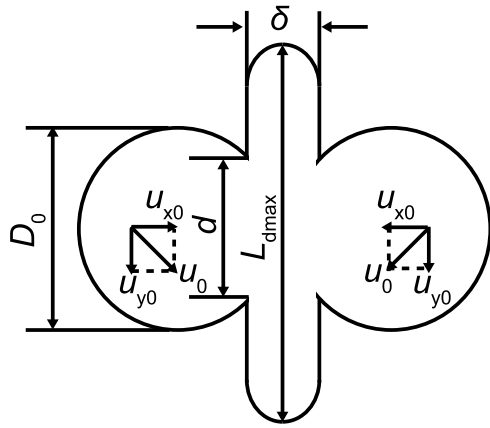


**Fig. 9.** Schematic diagram of the head-on collision of two droplets with size  $D_0$  and initial impact velocity  $u_0$  at the time of maximum spread.

By integrating the viscous dissipation rate over the droplet volume and time, the theoretical  $E_{\text{dis}}$  is given by

$$E_{\text{dis}} = \mu_l \int_0^{t_{\text{max}}} dt \int \frac{1}{2} \left( \frac{\partial u_x}{\partial y} + \frac{\partial u_y}{\partial x} \right)^2 (dx)^3 \quad (13)$$

Eq. (13) can be estimated to be [35]

$$E_{\text{dis}} \approx \mu_l \left( \frac{u_r}{\delta} \right)^2 (\pi d^2 \delta) t_{\text{max}} \quad (14)$$

where  $d$  varies between 0 and  $D_0$ , and is approximated to be  $D_0/2$  [1, 44]. As can be seen from Eq. (14),  $E_{\text{dis}}$  is linearly proportional to  $t_{\text{max}}$ , so the estimation of  $t_{\text{max}}$  is critical to the value of  $E_{\text{dis}}$ . Pan et al. [1] used  $t_{\text{max}} = (8D_0)/(3u_r)$  and obtained that  $E_{\text{dis}} \approx \pi \mu_l u_r L_{\text{dmax}}^2 / 4$ , and its viscous dissipation ratio  $\kappa_{\text{dis}} = E_{\text{dis}}/E_{\text{kx0}}$  is  $6\alpha_{\text{max}}/\text{Re}$ . Planchette et al. [32] showed that  $t_{\text{max}}$  is a fraction of one drop oscillation period  $t_{\text{oscill}} = \sqrt{\rho D_0^3/\sigma}$ , and scaled  $t_{\text{max}}$  with  $t_{\text{oscill}}$  for high  $We$  ( $> 50$ ) and with  $D_0/u_0$  for low  $We$  ( $< 50$ ). Therefore, for  $We > 200$ , using  $t_{\text{max}} = (8D_0)/(3u_r)$  to calculate  $E_{\text{dis}}$  could be inaccurate. Planchette et al. [32] proposed a general formula  $t_{\text{max}} = a(t_{\text{oscill}} + bD_0/u_0)$ , where  $a$  and  $b$  are the correction factors. Non-dimensionalize the formula by multiplying  $u_r/D_0$  yields

$$t_{\text{max}} = aWe^{0.5} + 2ab \quad (15)$$

We compare the experimental  $\tau_{\text{max}}$  of this study, Willis and Orme [3] and Planchette et al. [32], with the theoretical ones of Planchette et al. [32] and Pan et al. [1] under  $B \approx 0$  and various  $We$ , in Fig. 10(a). The experimental  $\tau_{\text{max}}$  stays larger than the theoretical one of Pan et al. [1], and the difference between them becomes larger as  $We$  increases, suggesting that  $E_{\text{dis}}$  is underestimated. On the contrary, the correlation  $\tau_{\text{max}} = aWe^{0.5} + 2ab$  proposed by Planchette et al. [32] agrees well with the experimental  $\tau_{\text{max}}$  with  $a = 0.3$  and  $b = 2$ .

By substituting Eq. (11),  $d = D_0/2$  and Eq. (15) in Eq. (14), we obtain

$$E_{\text{dis}} \approx \frac{3}{16} \pi \mu_l u_r L_{\text{dmax}}^2 (0.3We^{0.5} + 1.2) \quad (16)$$

and

$$\kappa_{\text{dis}} \approx \frac{9\alpha_{\text{max}}(0.3We^{0.5} + 1.2)}{2Re} \quad (17)$$

To verify Eq. (17), we compare the experimental  $\kappa_{\text{dis}}$  of this study, Willis and Orme [3], Planchette et al. [32] and Al-Dirawi et al. [38], with the theoretical ones of Eq. (17), Pan et al. [1] and Dai and Schmidt [18] in Fig. 10(b). It shows that as  $Oh < 0.025$ , the deviation of the theoretical  $\kappa_{\text{dis}}$  of Pan et al. [1] from the experimental ones is large, while Eq. (17) matches them well, suggesting a greatly improved prediction on viscous dissipation. However, as  $Oh > 0.025$ ,  $\kappa_{\text{dis}}$  of both Pan et al. [1] and Eq. (17) are greater than 1.3, which is inconsistent

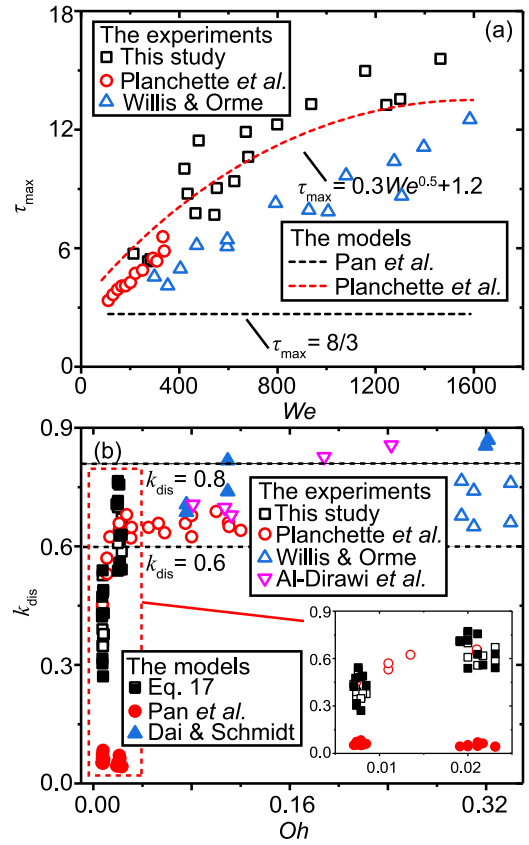


**Fig. 10.** (a) Comparison of the experimental dimensionless maximum spread time  $\tau_{\text{max}}$  of this study, Planchette et al. [32] and Willis and Orme [3], with the theoretical ones of Planchette et al. [32] and Pan et al. [1] under  $B \approx 0$  and various  $We$ . (b) Comparison of the experimental viscous dissipation ratio  $\kappa_{\text{dis}}$  of this study, Planchette et al. [32], Willis and Orme [3] and Al-Dirawi et al. [38], with the theoretical ones of Eq. (17), Pan et al. [1] and Dai and Schmidt [18] under  $B \approx 0$  and various  $Oh$ . The inset indicates the comparison of the experimental  $\kappa_{\text{dis}}$  of this study and Planchette et al. [32], with the theoretical ones of Eq. (17) and Pan et al. [1] under  $B \approx 0$  and  $0 < Oh < 0.025$ .

with the experiment, suggesting that Eq. (17) is mainly valid for  $Oh < 0.025$ . For  $Oh > 0.025$ ,  $\kappa_{\text{dis}}$  generally falls between 0.6 and 0.9 (see Fig. 10(b)). Thus,  $E_{\text{dis}}$  is obtained by Eq. (16) for  $Oh < 0.025$ , while  $E_{\text{dis}} = \kappa_{\text{dis}} E_{\text{kx0}}$  for  $Oh > 0.025$ .

For  $Oh < 0.025$ , by combining Eqs. (9), (12) and (16), we obtain the implicit expression of  $\alpha_{\text{max}}$

$$\left( \frac{1}{Ca} + \frac{9}{80} We^{0.5} + \frac{9}{20} \right) \alpha_{\text{max}}^3 - \left( \frac{4}{Ca} + \frac{Re}{12} \right) \alpha_{\text{max}} + \frac{8}{3Ca} = 0 \quad (18)$$

Similarly, for  $Oh > 0.025$ , by combining Eq. (9), Eq. (12) and  $E_{\text{dis}} = \kappa_{\text{dis}} E_{\text{kx0}}$ , we obtain

$$\alpha_{\text{max}}^3 - \left[ \frac{(1 - \kappa_{\text{dis}})}{12} We + 4 \right] \alpha_{\text{max}} + \frac{8}{3} = 0 \quad (19)$$

It is worth noting that Eq. (19) was also derived by Al-Dirawi et al. [38] based on energy conservation. To verify Eq. (18) and Eq. (19), in Fig. 11 we compare the theoretical  $\alpha_{\text{max}}$  of Eq. (18), Eq. (19) and Pan et al. [1], with the experimental ones of this study and Willis and Orme [3]. The experimental  $\alpha_{\text{max}}$  in this study corresponds to the collision of water droplets with  $0.007 < Oh < 0.0085$  and ethanol droplets with  $0.019 < Oh < 0.023$ , and the one of Willis and Orme [3] corresponds to the collision of Dow Corning 200 silicon-based oil droplets (DC200) with  $0.3 < Oh < 0.33$ . The prediction of  $\alpha_{\text{max}}$  is greatly improved for both water and ethanol droplets by using Eq. (18).  $t_{\text{max}}$  of Pan et al. [1] without considering the effect of  $t_{\text{oscill}}$  is less accurate at high  $We$ . The model of  $t_{\text{max}}$  proposed by Planchette

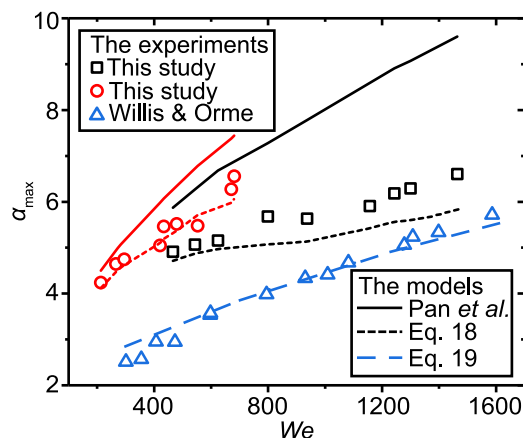


**Fig. 11.** Comparison of the theoretical maximum spread factor  $\alpha_{\max}$  of Pan et al. [1], Eqs. (18) and (19), with the experimental ones of this study and Willis and Orme [3] under various  $We$ . Water droplets with  $0.007 < Oh < 0.0085$  are marked in red, ethanol droplets with  $0.019 < Oh < 0.023$  in black, and Dow Corning 200 silicon-based oil droplets with  $0.3 < Oh < 0.33$  in blue.

et al. [32] greatly improves the prediction of  $E_{\text{dis}}$  and thus the one of  $\alpha_{\max}$  for water and ethanol featuring low  $Oh$ . For DC200 featuring high  $Oh$ , Fig. 11 shows that Eq. (19) at  $\kappa_{\text{dis}} = 0.8$  enables a good prediction of  $\alpha_{\max}$ . The comparison of the theoretical  $\alpha_{\max}$  of Eqs. (18) and (19) with the experimental ones also verifies that  $\alpha_{\max}$  is a function of  $Oh$ , as proposed by Planchette et al. [32].

#### 4. Conclusions

The collision dynamics of pure water droplets and pure ethanol droplets under  $200 \leq We < 2000$  were studied experimentally and theoretically. The effects of impact parameters, as well as surface tension and viscosity on droplet separation, fragmentation, and collision regime were investigated. Four distinct droplet regimes of reflection separation, stretching separation, finger separation and splashing were found. Deformation and fragmentation of the various collision regimes were increasingly intensified as  $We$  increased. Under the same  $We$ , due to the larger inertia force and smaller viscous force, water droplet collision was more likely to form finger separation and splashing regimes than ethanol droplet collision. Higher surface tension and viscous force reduced droplet deformation and fragmentation, and further changed the collision regime. Since the viscous dissipation ratio of droplet at the maximum spread moment was a function of  $Oh$ , the model of the maximum spread factor of the coalesced droplet varied under various  $Oh$ . For a low  $Oh$ , the maximum spread factor model was greatly optimized by using the improved viscous dissipation energy model via integrating the correlation of the maximum spread time proposed by Planchette et al. [32]. For a high  $Oh$ , the maximum spread factor model was developed by using the viscous dissipation ratio, and it agreed well with the experiment as the viscous dissipation ratio was 0.8.

#### CRediT authorship contribution statement

**Dongdong Zhou:** Conceptualization, Data curation, Investigation, Methodology, Visualization, Writing – original draft. **Xiufang Liu:** Investigation, Writing – review & editing. **Song Yang:** Investigation, Methodology, Writing – review & editing. **Yu Hou:** Investigation, Writing – review & editing. **Xin Zhong:** Conceptualization, Funding acquisition, Resources, Supervision, Writing – review & editing.

#### Declaration of competing interest

The authors declare that they have no known competing financial interests or personal relationships that could have appeared to influence the work reported in this paper.

#### Data availability

Data will be made available on request.

#### Acknowledgments

This work is supported by the National Natural Science Foundation of China (NO. 52076164, and NO. 51806163), the National Science and Technology Major Special Funds of China (NO. J2019-III-0010-0054) and the Fundamental Research Funds for the Central Universities, China (NO. ND6J005).

#### Appendix A. Supplementary data

Supplementary material related to this article can be found online at <https://doi.org/10.1016/j.colsurfa.2022.130171>.

#### References

- [1] K.L. Pan, P.C. Chou, Y.J. Tseng, Binary droplet collision at high Weber number, *Phys. Rev. E* 80 (2009) 036301.
- [2] K. Willis, M. Orme, Experiments on the dynamics of droplet collisions in a vacuum, *Exp. Fluids* 29 (2000) 347–358.
- [3] K. Willis, M. Orme, Binary droplet collisions in a vacuum environment: an experimental investigation of the role of viscosity, *Exp. Fluids* 34 (2003) 28–41.
- [4] J.M. Gac, L. Gradoñ, Lattice-Boltzmann modeling of collisions between droplets and particles, *Colloids Surf. A: Physicochem. Eng. Asp.* 441 (2014) 831–836.
- [5] K.G. Krishnan, E. Loth, Effects of gas and droplet characteristics on drop-drop collision outcome regimes, *Int. J. Multiph. Flow* 77 (2015) 171–186.
- [6] A. Amani, N. Balcázar, E. Gutiérrez, A. Oliva, Numerical study of binary droplets collision in the main collision regimes, *Chem. Eng. J.* 370 (2019) 477–498.
- [7] T. Wang, S.I. Andersen, A. Shapiro, Coalescence of oil droplets in microchannels under brine flow, *Colloids Surf. A: Physicochem. Eng. Asp.* 598 (2020) 124864.
- [8] M.R. Hassan, C. Wang, Ferro-hydrodynamic interactions between ferrofluid droplet pairs in simple shear flows, *Colloids Surf. A: Physicochem. Eng. Asp.* 602 (2020) 124906.
- [9] D. Zhou, X. Liu, S. Yang, Y. Hou, X. Zhong, Collision dynamics of two liquid nitrogen droplets under a low-temperature condition, *Cryogenics* 124 (2022) 103478.
- [10] Z. Zhang, P. Zhang, Cross-impingement and combustion of sprays in high-pressure chamber and opposed-piston compression ignition engine, *Appl. Therm. Eng.* 144 (2018) 137–146.
- [11] H. Montazeri, B. Blocken, J.L.M. Hensen, CFD analysis of the impact of physical parameters on evaporative cooling by a mist spray system, *Appl. Therm. Eng.* 75 (2015) 608–622.
- [12] J. Hempel, B. Tansel, S. Laha, Effect of temperature and pH on droplet aggregation and phase separation characteristics of flocs formed in oil-water emulsions after coagulation, *Colloids Surf. A: Physicochem. Eng. Asp.* 353 (2010) 37–42.
- [13] Y.R. Zhang, K.H. Luo, Regimes of head-on collisions of equal-sized binary droplets, *Langmuir* 35 (2019) 8896–8902.
- [14] G.S. Chaitanya, K.C. Sahu, G. Biswas, A study of two unequal-sized droplets undergoing oblique collision, *Phys. Fluids* 33 (2021) 022110.
- [15] A. Venkateshwarlu, R.P. Bharti, Interface evolution and pinch-off mechanism of droplet in two-phase liquid flow through T-junction microfluidic system, *Colloids Surf. A: Physicochem. Eng. Asp.* 642 (2022) 128536.
- [16] C. Planchette, E. Lorenceau, G. Brenn, Liquid encapsulation by binary collisions of immiscible liquid drops, *Colloids Surf. A: Physicochem. Eng. Asp.* 365 (2010) 89–94.
- [17] I.V. Roisman, C. Planchette, E. Lorenceau, G. Brenn, Binary collisions of drops of immiscible liquids, *J. Fluid Mech.* 690 (2012) 512–535.
- [18] M. Dai, D.P. Schmidt, Numerical simulation of head-on droplet collision: effect of viscosity on maximum deformation, *Phys. Fluids* 17 (2005) 041701.
- [19] H.C. Cong, L.J. Qian, Y.T. Wang, J.Z. Lin, Numerical simulation of the collision behaviors of binary unequal-sized droplets at high Weber number, *Phys. Fluids* 32 (2020) 103307.
- [20] L. Qian, H. Cong, C. Zhu, A numerical investigation on the collision behavior of polymer droplets, *Polymers* 12 (2020) 263.
- [21] G. Finotello, J.T. Padding, N.G. Deen, A. Jongsma, F. Innings, J.A.M. Kuipers, Effect of viscosity on droplet-droplet collisional interaction, *Phys. Fluids* 29 (2017) 067102.
- [22] J.-P. Estrade, H. Carentz, G. Lavergne, Y. Biscos, Experimental investigation of dynamic binary collision of ethanol droplets - a model for droplet coalescence and bouncing, *Int. J. Heat Fluid Flow* 20 (1999) 486–491.
- [23] C. Rabe, J. Malet, F. Feuillebois, Experimental investigation of water droplet binary collisions and description of outcomes with a symmetric Weber number, *Phys. Fluids* 22 (2010) 047101.

- [24] M. Kuschel, M. Sommerfeld, Investigation of droplet collisions for solutions with different solids content, *Exp. Fluids* 54 (2013) 1440.
- [25] M. Hirschler, G. Oger, U. Nienke, D. Le Touze, Modeling of droplet collisions using smoothed particle hydrodynamics, *Int. J. Multiph. Flow.* 95 (2017) 175–187.
- [26] K.L. Huang, K.L. Pan, Transitions of bouncing and coalescence in binary droplet collisions, *J. Fluid Mech.* 928 (2021) A7.
- [27] X. Chen, V. Yang, Direct numerical simulation of multiscale flow physics of binary droplet collision, *Phys. Fluids* 32 (2020) 062103.
- [28] M.A. Moqaddam, S.S. Chikatamarla, I.V. Karlin, Simulation of binary droplet collisions with the entropic lattice Boltzmann method, *Phys. Fluids* 28 (2016) 022106.
- [29] J. Qian, C.K. Law, Regimes of coalescence and separation in droplet collision, *J. Fluid Mech.* 331 (1997) 59–80.
- [30] N. Ashgriz, J.Y. Poo, Coalescence and separation in binary collisions of liquid drops, *J. Fluid Mech.* 221 (1990) 183–204.
- [31] C. Planchette, E. Lorenceau, G. Brenn, The onset of fragmentation in binary liquid drop collisions, *J. Fluid Mech.* 702 (2012) 5–25.
- [32] C. Planchette, H. Hinterbichler, M. Liu, D. Bothe, G. Brenn, Colliding drops as coalescing and fragmenting liquid springs, *J. Fluid Mech.* 814 (2017) 277–300.
- [33] D. Baumgartner, G. Brenn, C. Planchette, Universality of stretching separation, *J. Fluid Mech.* 937 (2022) R1.
- [34] M. Liu, D. Bothe, Numerical study of head-on droplet collisions at high Weber numbers, *J. Fluid Mech.* 789 (2016) 785–805.
- [35] Y.J. Jiang, A. Umemura, C.K. Law, An experimental investigation on the collision behaviour of hydrocarbon droplets, *J. Fluid Mech.* 234 (1992) 171–190.
- [36] G. Brenn, V. Kolobaric, Satellite droplet formation by unstable binary drop collisions, *Phys. Fluids* 18 (2006) 087101.
- [37] C. Gotaas, P. Havelka, H.A. Jakobsen, H.F. Svendsen, M. Hase, N. Roth, B. Weigand, Effect of viscosity on droplet-droplet collision outcome: Experimental study and numerical comparison, *Phys. Fluids* 19 (2007) 102106.
- [38] K.H. Al-Dirawi, K.H.A. Al-Ghaithi, T.C. Sykes, J.R. Castrejn-Pita, A.E. Bayly, Inertial stretching separation in binary droplet collisions, *J. Fluid Mech.* 927 (2021) A9.
- [39] C.G. Sedano, C.A. Aguirre, G.A. Rondan, A.B. Brizuela, Numerical simulation of spray ejection from a nozzle for herbicide application: evaporation and binary collision models, *Comput. Electron. Agr.* 175 (2020) 105551.
- [40] N.E. Shlegel, P.P. Tkachenko, P.A. Strizhak, Influence of viscosity, surface and interfacial tensions on the liquid droplet collisions, *Chem. Eng. Sci.* 220 (2020) 115639.
- [41] R.F. Allen, The role of surface tension in splashing, *J. Colloid Interf. Sci.* 51 (1975) 350–351.
- [42] N. Mehdizadeh, S. Chandra, J. Mostaghimi, Formation of fingers around the edges of a drop hitting a metal plate with high velocity, *J. Fluid Mech.* 510 (2004) 353–373.
- [43] I.V. Roisman, K. Horvat, C. Tropea, Spray impact: Rim transverse instability initiating fingering and splash, and description of a secondary spray, *Phys. Fluids* 18 (2006) 102104.
- [44] M. Pasandideh-Fard, Y.M. Qiao, S. Chandra, J. Mostaghimi, Capillary effects during droplet impact on a solid surface, *Phys. Fluids* 8 (1996) 650–659.